Continuum Skyrme-Hartree-Fock-Bogoliubov theory with Green's function method for odd-*A* nuclei

Ting-Ting Sun,* Zi-Xin Liu, Long Qian, Bing Wang, and Wei Zhang
School of Physics and Engineering, Zhengzhou University, Zhengzhou 450001, China

(Received 8 January 2019; published 14 May 2019)

To study exotic odd nuclear systems, the self-consistent continuum Skyrme-Hartree-Fock-Bogoliubov theory formulated with Green's function technique is extended to include blocking effects with the equal filling approximation. Detailed formulas are presented. By comparing with box-discretized calculations, the great advantages of the Green's function method in describing the extended density distributions, resonant states, and the couplings with the continuum in exotic nuclei are shown. Taking the neutron-rich odd nucleus ^{159}Sn as an example, the halo structure is investigated by blocking the lowest quasiparticle state. We find that it is mainly the weakly bound states near the Fermi surface that contribute a lot to the extended density distributions at large coordinate space. Finally, taking the neutron-rich Sn isotopes with mass numbers $A = 122$–178 as examples, the halo structures are studied systematically. The small two-neutron separation energy and the low Fermi energy in a long mass range after the shell $N = 82$ offer a good environment for the emergence of the halo structure. The neutron rms radius in ^{133}Sn and the heavier isotopes display a steep increase with A and deviate from the traditional rule of $r \propto A^{1/3}$. Correspondingly, the densities for those nuclei are very extended. Besides, the odd-even staggering of neutron radius $r_{\rm rms}$ is observed in the mass region $A = 151$–165, due to the occupations of the odd neutrons on the low p orbits.

DOI: 10.1103/PhysRevC.99.054316

I. INTRODUCTION

With the operation of new radioactive ion beam facilities worldwide [1–7] and developments in detection techniques, exotic nuclei far from the β stability line have become a very challenging topic and have attracted great interest experimentally and theoretically [8–16]. Many new and exotic phenomena such as halos [17–22], changes of nuclear magic numbers [23], and pygmy resonances [24] have been observed or predicted. In these weakly bound nuclei, the neutron or proton Fermi surface is very close to the continuum threshold, and the valence nucleons can be easily scattered to the continuum due to the pairing correlations. Besides, when the valence nucleons occupy states with low angular momentum, very extended spatial density distributions as well as large nuclear radius are obtained [20]. As a result, to give a proper theoretical description of the exotic nuclei, one must treat pairing correlations and the couplings with the continuum in a self-consistent way and consider properly the extended asymptotic behavior of nuclear density distributions.

The Hartree-Fock-Bogliubov (HFB) theory has achieved great successes in describing exotic nuclei with a unified description of the mean field and the pairing correlation and with proper treatment of the coupling with the continuum. In the spherical case, it has been mainly applied to the Gogny-HFB theory [25], Skyrme-HFB theory [26–29], the relativistic continuum Hartree-Bogoliubov (RCHB) theory [30–33], and density dependent relativistic Hartree-Fock-Bogoliubov (RHFB) theory [34–36]. To describe the halo phenomenon in deformed nuclei, the deformed relativistic Hartree-Bogoliubov (DRHB) theory based on a Woods-Saxon basis [22,37–40] and the coordinate-space Skyrme-HFB approach with interaction [41,42] have been developed. Generally, these H(F)B equations can be solved in the coordinate space [43] where the Nomerov or Runge-Kutta method [44] can be applied, or in an appropriate basis [45–47]. For the exotic nuclei with very extended density distributions, the simple oscillator basis fails due to its localized single-particle wave functions. Instead, the wave functions in a Woods-Saxon basis have a much more realistic asymptotic behavior at large coordinate. It is shown that the solutions of the relativistic Hartree equations in a Woods-Saxon basis is almost equivalent to the solution in coordinate space [47]. However, in the spherical systems, compared with the basis expansion method, solving the HFB equations in the coordinate space is more convenient.

In many calculations in the coordinate-space H(F)B approach, the box boundary condition is adopted, and hence the discretized quasiparticle states are obtained [20,27,31,48]. Although it is appropriate for deeply bound states, the box boundary condition is not suitable for weekly bound and continuum states unless a large enough box is taken. On the other hand, the Green's function method [49] allows one to impose the correct asymptotic behaviors on the wave functions, especially for the weakly bound and continuum states, and to calculate the densities.

*ttsunphy@zzu.edu.cn

The Green's function (GF) method [50–52] is an efficient tool for describing the continuum: the discrete bound states and the continuum can be treated on the same footing, both the energies and widths for the resonant states can be given directly, and the correct asymptotic behaviors for the wave functions can be described. Nonrelativistically and relativistically, there are already many applications of the GF method in nuclear physics to study the contribution of the continuum to the ground states and excited states. Nonrelativistically, in the spherical case, in 1987, Belyaev *et al.* constructed the Green's function in the Hartree-Fock-Bogoliubov (HFB) theory in the coordinate representation [49]. Afterwards, Matsuo applied this Green's function to the quasiparticle random-phase approximation (QRPA) [53], which was further used to describe the collective excitations coupled to the continuum [54–60], microscopic structures of monopole pair vibrational modes and associated two-neutron transfer amplitudes in neutron-rich Sn isotopes [61], and neutron capture reactions in the neutron-rich nuclei [62]. Recently, Zhang *et al.* developed the fully self-consistent continuum Skyrme-HFB theory with GF method [63–65]. In the deformed case, in 2009, Oba *et al.* extended the continuum HFB theory to include deformation on the basis of a coupled-channel representation and explored the properties of the continuum and pairing correlation in deformed nuclei near the neutron drip line [66]. Relativistically, in the spherical case, in Refs. [67,68], the fully self-consistent relativistic continuum random-phase-approximation (RCRPA) was developed with the Green's function of the Dirac equation and used to study the contribution of the continuum to nuclear collective excitations. In 2014, considering the great successes of the covariant density functional theory (CDFT) in nuclear structure [31,69–82] and nuclear astrophysics [83–87], the authors developed the continuum CDFT based on the GF method, with which the accurate energies and widths of the single-neutron resonant states were calculated for the first time [88]. This method has been further extended to describe single-particle resonances for protons [89] and Λ hyperons [90]. In 2016, further containing pairing correlation, the Green's function relativistic continuum Hartree-Bogoliubov (GF-RCHB) theory was developed, in which the continuum was treated exactly and the giant halo phenomena in neutron-rich Zr isotopes were studied [91].

However, the above Skyrme HFB theory with the Green's function method is only formulated for even-even nuclei [53,63,64,66,92]. To describe the exotic nuclear structure in neutron rich odd-A nuclei, the blocking effect has to be taken into account. In this work, we extend the continuum Skyrme-HFB theory with Green's function method to discuss odd-A nuclei by incorporating the blocking effect. In this way, pairing correlations, continuum, and blocking effects can be described consistently in the coordinate space.

The paper is organized as follows: In Sec. II, we introduce the formulation of the continuum Skyrme-HFB theory for odd-A nuclei using the Green's function technique. Numerical details and checks will be presented in Sec. III. After giving the results and discussions in Sec. IV, finally conclusions are drawn in Sec. V.

II. THEORETICAL FRAMEWORK

A. Coordinate-space Hartree-Fock-Bogoliubov theory

In the Hartree-Fock-Bogoliubov (HFB) theory, the pair correlated nuclear system is described in terms of independent quasiparticles [93]. In the coordinate space, the HFB equation for the quasiparticle state $\phi_i(\boldsymbol{r}\sigma)$ is written as [26]

$$\begin{pmatrix} h-\lambda & \tilde{h} \\ \tilde{h}^* & -h^*+\lambda \end{pmatrix}\phi_i(\boldsymbol{r}\sigma) = E_i\phi_i(\boldsymbol{r}\sigma), \tag{1}$$

with the quasiparticle energy E_i and the Fermi energy λ determined by constraining the expectation value of the nucleon number. The solutions of the HFB equation have two symmetric branches. One is positive ($E_i > 0$) with wave function $\phi_i(\boldsymbol{r}\sigma)$, and the other one is negative ($-E_i < 0$) with conjugate wave function $\bar{\phi}_{\bar{i}}(\boldsymbol{r}\sigma)$. The quasiparticle wave function $\phi_i(\boldsymbol{r}\sigma)$ and its conjugate wave function $\bar{\phi}_{\bar{i}}(\boldsymbol{r}\sigma)$ have two components,

$$\phi_i(\boldsymbol{r}\sigma) \equiv \begin{pmatrix} \varphi_{1,i}(\boldsymbol{r}\sigma) \\ \varphi_{2,i}(\boldsymbol{r}\sigma) \end{pmatrix}, \quad \bar{\phi}_{\bar{i}}(\boldsymbol{r}\sigma) \equiv \begin{pmatrix} -\varphi^*_{2,i}(\boldsymbol{r}\tilde{\sigma}) \\ \varphi^*_{1,i}(\boldsymbol{r}\tilde{\sigma}) \end{pmatrix}, \tag{2}$$

where $\varphi(\boldsymbol{r}\tilde{\sigma}) \equiv -2\sigma\varphi(\boldsymbol{r}, -\sigma)$. Note that the notations in this paper follow Ref. [53]. The Hartree-Fock Hamiltonian $h(\boldsymbol{r}\sigma, \boldsymbol{r}'\sigma')$ and the pair Hamiltonian $\tilde{h}(\boldsymbol{r}\sigma, \boldsymbol{r}'\sigma')$ can be respectively obtained by the variation of the total energy functional with respect to the particle density $\rho(\boldsymbol{r}\sigma, \boldsymbol{r}'\sigma')$ and pair density $\tilde{\rho}(\boldsymbol{r}\sigma, \boldsymbol{r}'\sigma')$,

$$\rho(\boldsymbol{r}\sigma, \boldsymbol{r}'\sigma') \equiv \langle\Phi_0|c^\dagger_{\boldsymbol{r}'\sigma'}c_{\boldsymbol{r}\sigma}|\Phi_0\rangle, \tag{3a}$$

$$\tilde{\rho}(\boldsymbol{r}\sigma, \boldsymbol{r}'\sigma') \equiv \langle\Phi_0|c_{\boldsymbol{r}'\tilde{\sigma}'}c_{\boldsymbol{r}\sigma}|\Phi_0\rangle, \tag{3b}$$

where $|\Phi_0\rangle$ is the ground state of the system and $c_{r\sigma}$ and $c^\dagger_{r\sigma}$ are the particle annihilate and creation operators, respectively. The two density matrices can be combined in a generalized density matrix R as

$$R(\boldsymbol{r}\sigma, \boldsymbol{r}'\sigma') \equiv \begin{pmatrix} \rho(\boldsymbol{r}\sigma, \boldsymbol{r}'\sigma') & \tilde{\rho}(\boldsymbol{r}\sigma, \boldsymbol{r}'\sigma') \\ \tilde{\rho}^*(\boldsymbol{r}\tilde{\sigma}, \boldsymbol{r}'\tilde{\sigma}') & \delta_{\boldsymbol{r}\boldsymbol{r}'}\delta_{\sigma\sigma'} - \rho^*(\boldsymbol{r}\tilde{\sigma}, \boldsymbol{r}'\tilde{\sigma}') \end{pmatrix}, \tag{4}$$

where the particle density $\rho(\boldsymbol{r}\sigma, \boldsymbol{r}'\sigma')$ and pair density $\tilde{\rho}(\boldsymbol{r}\sigma, \boldsymbol{r}'\sigma')$ are the "11" and "12" components of $R(\boldsymbol{r}\sigma, \boldsymbol{r}'\sigma')$, respectively.

For an even-even nucleus, the ground state $|\Phi_0\rangle$ is represented as a vacuum with respect to quasiparticles [93], i.e.,

$$\beta_i|\Phi_0\rangle = 0 \quad \text{for all } i = 1, \ldots, M, \tag{5}$$

where β_i and $\beta^\dagger_i$ are the quasiparticle annihilation and creation operators which are obtained by the Bogoliubov transformation from the particle operators $c_{r\sigma}$ and $c^\dagger_{r\sigma}$, and M is the dimension of the quasiparticle space.

Starting from the bare vacuum $|0\rangle$, the ground state $|\Phi_0\rangle$ for an even-even nucleus can be constructed as

$$|\Phi_0\rangle = \prod_i \beta_i|0\rangle, \tag{6}$$

where i runs over all values of $i = 1, 2, \ldots, M$.

With the quasiparticle vacuum $|\Phi_0\rangle$, the generalized density matrix can be expressed in a simple form,

$$R(\boldsymbol{r}\sigma,\boldsymbol{r}'\sigma') = \sum_{i:\text{all}} \bar{\phi}_{\bar{i}}(\boldsymbol{r}\sigma)\bar{\phi}^{\dagger}_{\bar{i}}(\boldsymbol{r}'\sigma'). \tag{7}$$

B. Blocking effect for odd-A nuclei

For an odd-A nucleus the ground state is a one-quasiparticle state $|\Phi_1\rangle$ [93], which can be constructed based on a HFB vacuum $|\Phi_0\rangle$ as

$$|\Phi_1\rangle = \beta^{\dagger}_{i_\text{b}}|\Phi_0\rangle, \tag{8}$$

where i_b denotes the blocked quasiparticle state occupied by the odd nucleon. For the ground state of the odd system, $\beta_{i_\text{b}} = \beta_1$ corresponds to the quasiparticle state with the lowest quasiparticle energy. The state $|\Phi_1\rangle$ is a vacuum to the operators $(\tilde{\beta}_{i_\text{b}}, \tilde{\beta}_2, \ldots, \tilde{\beta}_M)$ with

$$\tilde{\beta}_{i_\text{b}} = \beta^{\dagger}_1, \quad \tilde{\beta}_2 = \beta_2, \ldots, \tilde{\beta}_M = \beta_M, \tag{9}$$

where the exchange of the operators $\beta^{\dagger}_{i_\text{b}} \leftrightarrow \beta_{i_\text{b}}$ (or $\beta^{\dagger}_1 \leftrightarrow \beta_1$) corresponds to the exchange of the wave function

$$\phi_{i_\text{b}}(\boldsymbol{r}\sigma) \leftrightarrow \bar{\phi}_{\bar{i}_\text{b}}(\boldsymbol{r}\sigma). \tag{10}$$

Accordingly, the particle density $\rho(\boldsymbol{r}\sigma,\boldsymbol{r}'\sigma')$ and pair density $\tilde{\rho}(\boldsymbol{r}\sigma,\boldsymbol{r}'\sigma')$ for the one-quasiparticle state $|\Phi_1\rangle$ are

$$\rho(\boldsymbol{r}\sigma,\boldsymbol{r}'\sigma') \equiv \langle\Phi_1|c^{\dagger}_{\boldsymbol{r}'\sigma'}c_{\boldsymbol{r}\sigma}|\Phi_1\rangle, \tag{11a}$$

$$\tilde{\rho}(\boldsymbol{r}\sigma,\boldsymbol{r}'\sigma') \equiv \langle\Phi_1|c_{\boldsymbol{r}'\tilde{\sigma}'}c_{\boldsymbol{r}\sigma}|\Phi_1\rangle, \tag{11b}$$

and the generalized density matrix $R(\boldsymbol{r}\sigma,\boldsymbol{r}'\sigma')$ becomes

$$\begin{aligned} R(\boldsymbol{r}\sigma,\boldsymbol{r}'\sigma') = &\sum_{i:\text{all}} \bar{\phi}_{\bar{i}}(\boldsymbol{r}\sigma)\bar{\phi}^{\dagger}_{\bar{i}}(\boldsymbol{r}'\sigma') \\ &- \bar{\phi}_{\bar{i}_\text{b}}(\boldsymbol{r}\sigma)\bar{\phi}^{\dagger}_{\bar{i}_\text{b}}(\boldsymbol{r}'\sigma') + \phi_{i_\text{b}}(\boldsymbol{r}\sigma)\phi^{\dagger}_{i_\text{b}}(\boldsymbol{r}'\sigma'), \end{aligned} \tag{12}$$

where two more terms are introduced compared with those for even-even nuclei in Eq. (7) after including the blocking effect in odd nuclear systems.

C. Density and quasiparticle spectrum

In the conventional Skyrme-HFB theory, one solves the HFB equation (1) with the box boundary condition to obtain the discretized eigensolutions for the single-quasiparticle energy and the corresponding wave functions. Then the generalized density matrix $R(\boldsymbol{r}\sigma,\boldsymbol{r}'\sigma')$ can be constructed by a sum over discretized quasiparticle states. We call this method the box-discretized Skyrme-HFB approach. However, the box boundary condition is not appropriate for the description of weakly bound states and continuum in exotic nuclei unless a large enough box size is taken.

Instead, the Green's function method is used to impose the correct asymptotic behaviors on the wave functions, especially for the continuum states, and to calculate the densities. The Green's function $G(\boldsymbol{r}\sigma,\boldsymbol{r}'\sigma';E)$ with an arbitrary energy E defined for the coordinate-space HFB equation obeys

$$\begin{aligned} &\left[E - \begin{pmatrix} h-\lambda & \tilde{h} \\ \tilde{h}^* & -h^*+\lambda \end{pmatrix}\right] G(\boldsymbol{r}\sigma,\boldsymbol{r}'\sigma';E) \\ &\quad = \delta(\boldsymbol{r}-\boldsymbol{r}')\delta_{\sigma\sigma'}. \end{aligned} \tag{13}$$

With a complete set of eigenstates $\{\phi_i(\boldsymbol{r}\sigma), \bar{\phi}_{\bar{i}}(\boldsymbol{r}\sigma)\}$ and eigenvalues $\{E_i, -E_i\}$ of the HFB equation, the HFB Green's function in Eq. (13) can be represented as

$$\begin{aligned} &G(\boldsymbol{r}\sigma,\boldsymbol{r}'\sigma';E) \\ &\quad = \sum\!\!\!\!\!\!\int \left(\frac{\phi_i(\boldsymbol{r}\sigma)\phi^{\dagger}_i(\boldsymbol{r}'\sigma')}{E-E_i} + \frac{\bar{\phi}_{\bar{i}}(\boldsymbol{r}\sigma)\bar{\phi}^{\dagger}_{\bar{i}}(\boldsymbol{r}'\sigma')}{E+E_i}\right), \end{aligned} \tag{14}$$

which has two branches. One is for $\phi_i(\boldsymbol{r}\sigma)$ and E_i, and the other is for $\bar{\phi}_{\bar{i}}(\boldsymbol{r}\sigma)$ and $-E_i$. The $\sum\!\!\!\!\!\!\int$ is summation for the quasiparticle discrete states with the quasiparticle energy $|E_i| < |\lambda|$ and integral for the continuum with $|E_i| > |\lambda|$ explicitly.

Corresponding to the upper and lower components of the quasiparticle wave function, the Green's function for the HFB equation can be written as a 2×2 matrix,

$$G(\boldsymbol{r}\sigma,\boldsymbol{r}'\sigma';E) = \begin{pmatrix} G^{(11)}(E) & G^{(12)}(E) \\ G^{(21)}(E) & G^{(22)}(E) \end{pmatrix}. \tag{15}$$

Starting from Eq. (14) and according to Cauchy's theorem, the generalized density matrix in Eq. (12) can be calculated with the integrals of the Green's function in the complex quasiparticle energy plane as

$$\begin{aligned} R(\boldsymbol{r}\sigma,\boldsymbol{r}'\sigma') = \frac{1}{2\pi i}\Bigg[&\oint_{C_{E<0}} dE\, G(\boldsymbol{r}\sigma,\boldsymbol{r}'\sigma';E) \\ &- \oint_{C^-_\text{b}} dE\, G(\boldsymbol{r}\sigma,\boldsymbol{r}'\sigma';E) \\ &+ \oint_{C^+_\text{b}} dE\, G(\boldsymbol{r}\sigma,\boldsymbol{r}'\sigma';E)\Bigg], \end{aligned} \tag{16}$$

where the contour path $C_{E<0}$ encloses all the negative quasiparticle energies $-E_i$, C^-_b encloses only the pole $-E_{i_\text{b}}$, and C^+_b encloses only the pole E_{i_b}, which can be seen in Fig. 1. Note that the three terms in Eq. (16) corresponds one-to-one to those in Eq. (12). The energies E in $G(\boldsymbol{r}\sigma,\boldsymbol{r}'\sigma';E)$ are complex, taken along the paths $C_{E<0}$, C^-_b, and C^+_b.

In the spherical case, the quasiparticle wave function $\phi_i(\boldsymbol{r}\sigma)$ and the conjugate wave function $\bar{\phi}_{\bar{i}}(\boldsymbol{r}\sigma)$ can be expanded as

$$\phi_i(\boldsymbol{r}\sigma) = \frac{1}{r}\phi_{nlj}(r)Y^l_{jm}(\hat{\boldsymbol{r}}\sigma), \quad \phi_{nlj}(r) = \begin{pmatrix} \varphi_{1,nlj}(r) \\ \varphi_{2,nlj}(r) \end{pmatrix}, \tag{17a}$$

$$\bar{\phi}_{\bar{i}}(\boldsymbol{r}\sigma) = \frac{1}{r}\bar{\phi}_{nlj}(r)Y^{l*}_{jm}(\hat{\boldsymbol{r}}\tilde{\sigma}), \quad \bar{\phi}_{nlj}(r) = \begin{pmatrix} -\varphi^*_{2,nlj}(r) \\ \varphi^*_{1,nlj}(r) \end{pmatrix}, \tag{17b}$$

where $Y^l_{jm}(\hat{\boldsymbol{r}}\sigma)$ is the spin spherical harmonic, and $Y^l_{jm}(\hat{\boldsymbol{r}}\tilde{\sigma}) = -2\sigma Y^l_{jm}(\hat{\boldsymbol{r}}-\sigma)$. Similarly, the generalized density matrix $R(\boldsymbol{r}\sigma,\boldsymbol{r}'\sigma')$ and the Green's function $G(\boldsymbol{r}\sigma,\boldsymbol{r}'\sigma';E)$ can also be expanded as

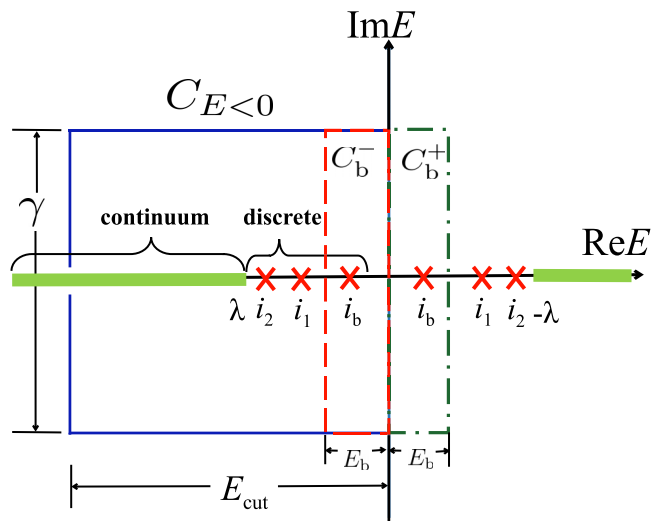

FIG. 1. Contour paths $C_{E<0}, C_{\rm b}^-, C_{\rm b}^+$ are to perform the integrations of the Green's function on the complex quasiparticle energy plane. The paths are chosen to be rectangles with the same width γ and different lengths, i.e., $E_{\rm cut}$, $E_{\rm b}$, and $E_{\rm b}$ for $C_{E<0}$, $C_{\rm b}^-$, and $C_{\rm b}^+$ respectively. The crosses denote the discrete quasiparticle states and the continuum states are denoted by the thick solid line. Quantum number $i_{\rm b}$ denotes the single quasiparticle state to be blocked.

$$R(\boldsymbol{r}\sigma,\boldsymbol{r}'\sigma') = \sum_{ljm} Y^l_{jm}(\hat{\boldsymbol{r}}\sigma) R_{lj}(r,r') Y^{l*}_{jm}(\hat{\boldsymbol{r}}'\sigma'), \tag{18a}$$

$$G(\boldsymbol{r}\sigma,\boldsymbol{r}'\sigma';E) = \sum_{ljm} Y^l_{jm}(\hat{\boldsymbol{r}}\sigma) \frac{\mathcal{G}_{lj}(r,r';E)}{rr'} Y^{l*}_{jm}(\hat{\boldsymbol{r}}'\sigma'), \tag{18b}$$

where $R_{lj}(r,r')$ and $\mathcal{G}_{lj}(r,r';E)$ are the radial parts of the generalized density matrix and Green's function, respectively. Note that the equal filling approximation is applied for the odd nucleon, i.e., we take an average of the blocked quasiparticle state $i_{\rm b} = (n_{\rm b} l_{\rm b} j_{\rm b} m_{j_{\rm b}})$ over the magnetic quantum numbers $m_{j_{\rm b}} = -j_{\rm b}, -j_{\rm b}+1, \ldots, j_{\rm b}-1, j_{\rm b}$.

As a result, the radial local generalized density matrix $R(r) = R(r,r)$ can be expressed by the radial box-discretized quasiparticle wave functions $\phi_{nlj}(r)$ or the radial HFB Green's function $\mathcal{G}_{lj}(r,r';E)$ as

$$\begin{aligned} R(r) &= \sum_{lj} R_{lj}(r,r) = \frac{1}{4\pi r^2}\Bigg[\sum_{lj:\rm all}(2j+1)\sum_{n:\rm all}\bar{\phi}^2_{nlj}(r) \\ &\quad - \bar{\phi}^2_{n_{\rm b}l_{\rm b}j_{\rm b}}(r) + \phi^2_{n_{\rm b}l_{\rm b}j_{\rm b}}(r)\Bigg] \\ &= \frac{1}{4\pi r^2}\frac{1}{2\pi i}\Bigg[\sum_{lj:\rm all}(2j+1)\oint_{C_{E<0}} dE\, \mathcal{G}_{lj}(r,r;E) \\ &\quad - \oint_{C_{\rm b}^-} dE \mathcal{G}_{l_{\rm b}j_{\rm b}}(r,r;E) + \oint_{C_{\rm b}^+} dE\, \mathcal{G}_{l_{\rm b}j_{\rm b}}(r,r;E)\Bigg]. \end{aligned} \tag{19}$$

From the radial generalized matrix $R(r)$, one can easily obtain the radial local particle density $\rho(r)$ and pair density $\tilde{\rho}(r)$, which are the "11" and "12" components of $R(r)$, respectively. In the same way, one can express other radial local densities needed in the functional of the Skyrme interaction [94,95], such as the kinetic-energy density $\tau(r)$, the spin-orbit density $J(r)$, etc., in terms of the radial Green's function.

Accordingly, the particle density and pair density for the blocked partial wave $lj = l_{\rm b}j_{\rm b}$ can be written as

$$\begin{aligned} \rho_{lj}(r) &= \rho_{0,lj}(r) - \rho_{1,lj}(r) + \rho_{2,lj}(r) \\ &= \frac{1}{4\pi r^2}\Bigg[(2j+1)\sum_n \varphi^2_{2,nlj}(r) - \varphi^2_{2,n_{\rm b}l_{\rm b}j_{\rm b}}(r) + \varphi^2_{1,n_{\rm b}l_{\rm b}j_{\rm b}}(r)\Bigg] \\ &= \frac{1}{4\pi r^2}\frac{1}{2\pi i}\Bigg[(2j+1)\oint_{C_E<0} dE\, \mathcal{G}^{(11)}_{lj}(r,r;E) - \oint_{C_{\rm b}^-} dE\, \mathcal{G}^{(11)}_{lj}(r,r;E) + \oint_{C_{\rm b}^+} dE\, \mathcal{G}^{(11)}_{lj}(r,r;E)\Bigg], \end{aligned} \tag{20a}$$

$$\begin{aligned} \tilde{\rho}_{lj}(r) &= \tilde{\rho}_{0,lj}(r) - \tilde{\rho}_{1,lj}(r) + \tilde{\rho}_{2,lj}(r) \\ &= \frac{1}{4\pi r^2}\Bigg[(2j+1)\sum_n \varphi_{1,nlj}(r)\varphi_{2,nlj}(r) - \varphi_{1,n_{\rm b}l_{\rm b}j_{\rm b}}(r)\varphi_{2,n_{\rm b}l_{\rm b}j_{\rm b}}(r) - \varphi_{2,n_{\rm b}l_{\rm b}j_{\rm b}}(r)\varphi_{1,n_{\rm b}l_{\rm b}j_{\rm b}}(r)\Bigg] \\ &= \frac{1}{4\pi r^2}\frac{1}{2\pi i}\Bigg[(2j+1)\oint_{C_E<0} dE\, \mathcal{G}^{(12)}_{lj}(r,r;E) - \oint_{C_{\rm b}^-} dE\, \mathcal{G}^{(12)}_{lj}(r,r;E) + \oint_{C_{\rm b}^+} dE\, \mathcal{G}^{(12)}_{lj}(r,r;E)\Bigg]. \end{aligned} \tag{20b}$$

And for the partial waves with $lj \neq l_{\rm b}j_{\rm b}$, the terms introduced by the blocking effect, i.e., $\rho_{1,lj}(r)$ and $\rho_{2,lj}(r)$ in $\rho_{lj}(r)$, and $\tilde{\rho}_{1,lj}(r)$ and $\tilde{\rho}_{2,lj}(r)$ in $\tilde{\rho}_{lj}(r)$, are zero.

Within the framework of the continuum Skyrme-HFB theory, the quasiparticle energy spectrum can be given by the occupation number density $n_{lj}(E)$ or the pair number density $\tilde{n}_{lj}(E)$. The integrals of them with energy E represent the occupied nucleon number N_{lj} and paired nucleon number $\tilde{N}_{lj}$ in partial wave lj, i.e.,

$$N_{lj} = \int dE\, n_{lj}(E), \tag{21a}$$

$$\tilde{N}_{lj} = \int dE\, \tilde{n}_{lj}(E). \tag{21b}$$

For odd-A nuclei, the occupation number density $n_{lj}(E)$ and the pair number density $\tilde{n}_{lj}(E)$ for the partial wave $lj = l_{\rm b}j_{\rm b}$ can be written as

$$\begin{aligned} n_{lj}(E) &= n_{0,lj}(E) - n_{1,lj}(E) + n_{2,lj}(E) \\ &= \frac{2j+1}{\pi}\int dr\,\mathrm{Im}\,\mathcal{G}^{(11)}_{0,lj}(r,r;-E-i\epsilon)\Big|^{0}_{-E=-E_{\rm cut}} \\ &\quad -\frac{1}{\pi}\int dr\,\mathrm{Im}\,\mathcal{G}^{(11)}_{l_{\rm b}j_{\rm b}}(r,r;-E-i\epsilon)\Big|^{0}_{-E=-E_{\rm b}} \\ &\quad +\frac{1}{\pi}\int dr\,\mathrm{Im}\,\mathcal{G}^{(11)}_{l_{\rm b}j_{\rm b}}(r,r;E-i\epsilon)\Big|^{E_{\rm b}}_{E=0}, \end{aligned} \tag{22a}$$

$$\begin{aligned} \tilde{n}_{lj}(E) &= \tilde{n}_{0,lj}(E) - \tilde{n}_{1,lj}(E) + \tilde{n}_{2,lj}(E) \\ &= \frac{2j+1}{\pi}\int dr\,\mathrm{Im}\,\mathcal{G}^{(12)}_{0,lj}(r,r;-E-i\epsilon)\Big|^{0}_{-E=-E_{\rm cut}} \\ &\quad -\frac{1}{\pi}\int dr\,\mathrm{Im}\,\mathcal{G}^{(12)}_{l_{\rm b}j_{\rm b}}(r,r;-E-i\epsilon)\Big|^{0}_{-E=-E_{\rm b}} \\ &\quad +\frac{1}{\pi}\int dr\,\mathrm{Im}\,\mathcal{G}^{(12)}_{l_{\rm b}j_{\rm b}}(r,r;E-i\epsilon)\Big|^{E_{\rm b}}_{E=0}, \end{aligned} \tag{22b}$$

where the terms $n_{1,lj}(E)$ and $n_{2,lj}(E)$ in $n_{lj}(E)$ and $\tilde{n}_{1,lj}(E)$ and $\tilde{n}_{2,lj}(E)$ in $\tilde{n}_{lj}(E)$ are introduced due to the blocking effect, and they are zero for the partial waves with $lj \neq l_{\rm b}j_{\rm b}$, and ϵ is the smoothing parameter with which the δ function originating from a discrete quasiparticle state is simulated by a Lorentzian function with the full-width at half-maximum of 2ϵ. The energy ranges of the Green's functions in the terms $n_{0,lj}(E)$, $n_{1,lj}(E)$, and $n_{2,lj}(E)$ are $-E_{\rm cut} < -E < 0$, $-E_{\rm b} < -E < 0$, and $0 < E < E_{\rm b}$, which are in accordance with the real energy ranges of the contour paths $C_{E<0}$, $C_{\rm b}^{-}$, and $C_{\rm b}^{+}$ in Fig. 1.

D. Construction of HFB Green's function

For given quasiparticle energy E and quantum number lj, the radial HFB Green's function $\mathcal{G}_{lj}(r,r';E)$ can be constructed as

$$\begin{aligned} \mathcal{G}_{lj}(r,r';E) = \sum_{s,s'=1,2} c^{ss'}_{lj}\big[&\theta(r-r')\phi^{(+s)}_{lj}(r,E)\phi^{(rs')T}_{lj}(r',E) \\ &+ \theta(r'-r)\phi^{(rs')}_{lj}(r,E)\phi^{(+s)T}_{lj}(r',E)\big], \end{aligned} \tag{23}$$

where $\theta(r-r')$ is the step function, $\phi^{(rs)}_{lj}(r,E)$ and $\phi^{(+s)}_{lj}(r,E)$ ($s=1,2$) are independent solutions of the radial HFB equations,

$$\begin{aligned} \phi^{(rs)}_{lj}(r,E) &= \begin{pmatrix} \varphi^{(rs)}_{1,lj}(r,E) \\ \varphi^{(rs)}_{2,lj}(r,E) \end{pmatrix}, \\ \phi^{(+s)}_{lj}(r,E) &= \begin{pmatrix} \varphi^{(+s)}_{1,lj}(r,E) \\ \varphi^{(+s)}_{2,lj}(r,E) \end{pmatrix}, \end{aligned} \tag{24}$$

obtained by a Runge-Kutta integral starting from the boundary conditions at the origin, $r=0$, and at the edge of the box, $r=R$, respectively. The coefficients $c^{ss'}_{lj}(E)$ are expressed in terms of the Wronskians as

$$\begin{pmatrix} c^{11}_{lj} & c^{12}_{lj} \\ c^{21}_{lj} & c^{22}_{lj} \end{pmatrix} = \begin{pmatrix} w_{lj}(r1,+1) & w_{lj}(r1,+2) \\ w_{lj}(r2,+1) & w_{lj}(r2,+2) \end{pmatrix}^{-1}, \tag{25}$$

with

$$\begin{aligned} &w_{lj}(rs,+s') \\ &= \frac{\hbar^2}{2m}\Big[\varphi^{(rs)}_{1,lj}(r)\frac{d}{dr}\varphi^{(+s')}_{1,lj}(r) - \varphi^{(+s')}_{1,lj}(r)\frac{d}{dr}\varphi^{(rs)}_{1,lj}(r) \\ &\quad -\varphi^{(rs)}_{2,lj}(r)\frac{d}{dr}\varphi^{(+s')}_{2,lj}(r) + \varphi^{(+s')}_{2,lj}(r)\frac{d}{dr}\varphi^{(rs)}_{2,lj}(r)\Big]. \end{aligned} \tag{26}$$

Note that the energies E and the solutions $\phi^{(rs)}_{lj}(r,E)$ and $\phi^{(+s)}_{lj}(r,E)$ in the constructed Green's function (23) are not eigenvalues and eigenfunctions of the HFB equation.

To impose the correct asymptotic behavior on the wave function for the continuum states, we adopt the boundary condition as follows:

$$\begin{aligned} &\phi^{(rs)}_{lj}(r,E)\,\text{: regular at the origin } r=0, \\ &\phi^{(+s)}_{lj}(r,E)\,\text{: outgoing wave at } r\to\infty. \end{aligned} \tag{27}$$

Explicitly, the solutions $\phi^{(+s)}_{lj}(r,E)$ at $r > R$ satisfy

$$\phi^{(+1)}_{lj}(r,E) \to \begin{pmatrix} e^{ik_+(E)r} \\ 0 \end{pmatrix}, \quad \phi^{(+2)}_{lj}(r,E) \to \begin{pmatrix} 0 \\ e^{ik_-(E)r} \end{pmatrix}. \tag{28}$$

Here $k_\pm(E) = \sqrt{2m(\lambda \pm E)}/\hbar$ with m the nucleon mass, and their branch cuts are chosen so that $\mathrm{Im}\,k_\pm > 0$ is satisfied.

III. NUMERICAL DETAILS AND CHECKS

In this part, numerical details and checks in the continuum Skyrme-HFB calculations are presented for odd nuclear systems. Besides, the advantages of the Green's function method are shown compared with those by the discretized method with box boundary conditions.

A. Numerical details

In the particle-hole channel, the Skyrme parameter SLy4 [96] is taken. In the particle-particle channel, a density dependent δ interaction (DDDI) is adopted for the pairing interaction,

$$v_{\rm pair}(\boldsymbol{r},\boldsymbol{r}') = \frac{1}{2}(1-P_\sigma)V_0\left[1-\eta\left(\frac{\rho(\boldsymbol{r})}{\rho_0}\right)^{\alpha}\right]\delta(\boldsymbol{r}-\boldsymbol{r}'), \tag{29}$$

with which the pair Hamiltonian $\tilde{h}(\boldsymbol{r}\sigma,\boldsymbol{r}'\sigma')$ is reduced to a local pair potential [26]

$$\Delta(\boldsymbol{r}) = \frac{1}{2}V_0\left[1-\eta\left(\frac{\rho(\boldsymbol{r})}{\rho_0}\right)^{\alpha}\right]\tilde{\rho}(\boldsymbol{r}), \tag{30}$$

where $\rho(\boldsymbol{r})$ and $\tilde{\rho}(\boldsymbol{r})$ are the particle density and pair density, respectively. The parameters in DDDI are taken as $V_0 = -458.4$ MeV fm^3, $\eta = 0.71$, $\alpha = 0.59$, and $\rho_0 = 0.08$ fm^{-3}, which are constrained by reproducing the experimental neutron pairing gaps for the Sn isotopes [56,59,97] and the scattering length $a = -18.5$ fm in the ^1S channel of the bare nuclear force in the low density limit [97]. The cutoff of the quasiparticle states is taken with maximal angular momentum $j_{\rm max} = 25/2$ and the maximal quasiparticle energy $E_{\rm cut} = 60$ MeV. The smoothing parameter ϵ is Eq. (22) is taken

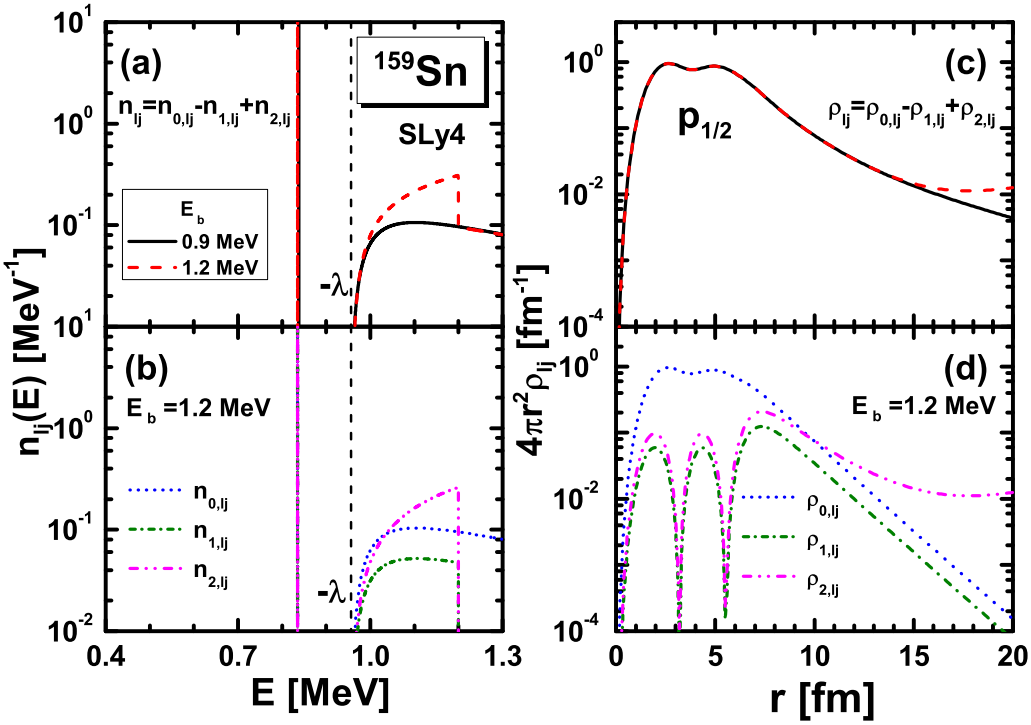

FIG. 2. (a) Neutron occupation number density $n_{lj}(E)$ around the continuum threshold energy $-\lambda$ and (b) neutron density distributions $4\pi r^2\rho_{lj}(r)$ for the partial wave $p_{1/2}$ of ^{159}Sn obtained in the continuum Skyrme HFB calculation by blocking quasiparticle state $3p_{1/2}$ with different blocking energy widths $E_b = 0.9$ MeV (solid lines) and 1.2 MeV (dashed lines). For the case of the blocking energy width $E_b > -\lambda$, i.e., $E_b = 1.2$ MeV, (b) the contributions for $n_{lj}(E)$ from the terms $n_{0,lj}(E)$, $n_{1,lj}(E)$, and $n_{2,lj}(E)$ in Eq. (22a), and (d) the contributions for $\rho_{lj}(r)$ from the terms $\rho_{0,lj}(r)$, $\rho_{1,lj}(r)$, and $\rho_{2,lj}(r)$ in Eq. (20a) are presented.

as 5 keV to discuss the structure of the occupation number density and pair number density.

To perform the integrals of the Green's function, the contour paths $C_{E<0}, C_b^-, C_b^+$ are chosen to be three rectangles on the complex quasiparticle energy plane as shown in Fig. 1, with the same height $\gamma = 0.1$ MeV and different widths, i.e., $E_{\rm cut}$, E_b, E_b respectively [63]. To enclose all the negative quasiparticle energies, the length of the contour path $C_{E<0}$ is taken as the maximal quasiparticle energy $E_{\rm cut} = 60$ MeV. The contour paths C_b^+ and C_b^- are symmetric with respect to the origin and have the same length E_b, which enclose the blocked quasiparticle states at E_{i_b} and $-E_{i_b}$, respectively. For the contour integration, we adopt an energy step $\Delta E = 0.01$ MeV on the contour path. In Fig. 1, the blocked state is the lowest quasiparticle state, corresponding to the ground state of the odd system. If one blocks a state with $i_1 < i_b < i_2$, the path $C_{E<0}$ keeps the same, while the paths C_b^- and C_b^+ introduced for the blocking effects should only include exactly the blocked state i_b. The HFB equation is solved with the box size $R = 20$ fm and mesh size $\Delta r = 0.1$ fm in the coordinate space.

B. Numerical checks

In the following, taking the odd-even neutron-rich nucleus ^{159}Sn as an example, the numerical checks on the widths of contour paths C_b^- and C_b^+ introduced due to the blocking effects will be discussed. As we have said, C_b^- and C_b^+ should include the pole of quasiparticle energy for the blocked level and the width E_b cannot be taken arbitrarily. In the following discussions, we mainly take two different blocking energy widths E_b, i.e., (1) $E_{i_b} < E_b < -\lambda$, and (2) $E_b > -\lambda$, where E_{i_b} is the quasiparticle energy of blocked level and $-\lambda$ is the continuum threshold. Both of them include the blocked level, but in the second case some continuum states are included in the contour paths C_b^- and C_b^+.

For the ground state of even-even nucleus ^{158}Sn, according to the continuum Skyrme-HFB calculations, the lowest quasiparticle state is $3p_{1/2}$ with the energy around 0.9 MeV and the Fermi energy around -1.0 MeV. Thus, in the calculations for the nearby odd-even nucleus ^{159}Sn with the Green's function method, the odd neutron will be blocked on the quasiparticle state $3p_{1/2}$ and we take $E_b = 0.9$ and 1.2 MeV for discussions of the blocking energy widths.

In Fig. 2, the neutron occupation number density $n_{lj}(E)$ around the continuum threshold energy $-\lambda$ and the neutron density distributions $4\pi r^2\rho_{lj}(r)$ for the blocked partial wave $p_{1/2}$ of ^{159}Sn are presented, which are calculated by the continuum Skyrme HFB with the blocking energy widths $E_b = 0.9$ and 1.2 MeV. From the occupation number density $n_{lj}(E)$ in panel (a), a discrete quasiparticle state $3p_{1/2}$ is observed around $E = 0.83$ MeV below the continuum threshold $-\lambda$, and very small continuum states in the region above $-\lambda$. Comparing the results obtained with $E_b = 0.9$ and 1.2 MeV, most of them are same except that an unphysical peak is observed in the continuum region in the case of $E_b = 1.2$ MeV, which

starts from the threshold energy $E = -\lambda$ and ends at $E = 1.2$ MeV. To analyze the structure of this unphysical peak, we plot in panel (b) the different contributions $n_{0,lj}(E)$, $n_{1,lj}(E)$, and $n_{2,lj}(E)$ in Eq. (22a) and find that it is the term $n_{2,lj}(E)$ that leads to the unphysical peak in continuum. A similar problem happens also for the neutron density distributions in the coordinate space. It can be seen in panel (c) that when the blocking energy width $E_b = 1.2$ MeV, the neutron density $4\pi r^2 \rho_{lj}(r)$ for the partial wave $p_{1/2}$ has an increasing tail compared with that obtained with $E_b = 0.9$ MeV, which is against the outgoing decay asymptotic behavior of the nuclear wave functions. To explain the abnormal tail of density, the contributions $\rho_{0,lj}(r)$, $\rho_{1,lj}(r)$, and $\rho_{2,lj}(r)$ in Eq. (20a) for $\rho_{lj}(r)$ are plotted in panel (d), and obviously it is caused by the term $\rho_{2,lj}(r)$. However, the unphysical peak in $n_{lj}(E)$ and increasing tail in $\rho_{lj}(r)$ do not happen when taking any blocking energy width if $E_b < -\lambda$. Thus, we can explain these problems as following: in the case of $E_b = 1.2$ MeV, extra continuum distributed over the threshold $-\lambda$ is included in blocking. For the quasiparticle states in continuum, the upper component of the wave function $\varphi_1(r)$ is oscillating and outgoing while the lower component $\varphi_2(r)$ is decaying. Since the term $\rho_{2,lj}(r)$ in Eq. (20a) is related to $\varphi^2_{1,n_b l_b j_b}(r)$, the calculated density will be oscillating and outgoing in large coordinate if continuum states are included. A similar explanation is applicable for the occupation number density $n_{2,lj}(E)$, which is also related to $\varphi^2_{1,n_b l_b j_b}(r)$.

According to the above discussions, in the following the blocking energy width E_b should be taken with $E_{i_b} < E_b < -\lambda$. However, note that for the very neutron rich nuclei whose Fermi surface is very close to zero, there maybe no discrete quasiparticle states and we have to block a quasiparticle state in continuum. In this case, the blocking contour path will intrude into the continuum and should be taken very carefully, including only the blocked level.

In the following, we will show the advantages of the Green's function method in describing the neutron-rich nuclei compared with using the box-discretized method. In Fig. 3, the particle density $\rho_n(r)$ and pair density $\tilde{\rho}_n(r)$ for neutrons in ^{159}Sn obtained in the continuum and box-discretized Skyrme-HFB calculations are presented with coordinate space sizes of $R = 15$ fm and $R = 20$ fm, respectively. It can be clearly seen that in the box-discretized calculations, densities $\rho_n(r)$ and $\tilde{\rho}_n(r)$ in ^{159}Sn decrease sharply at the edge due to the box boundary conditions, which restrict wave functions to zero at the edge of the box. As a result, in order to describe the asymptotic behaviors of extended density distributions properly, large coordinate space size should be taken. However, in the continuum Skyrme-HFB calculations with Green's function method, the exponential decay of density distribution is well described. Moreover, these descriptions are independent of the space size because the correct asymptotic behaviors on the wave functions, especially for the continuum states, are imposed in the Green's function method to describe extended densities.

In Fig. 4, the occupation number density $n_{lj}(E)$ and pair number density $\tilde{n}_{lj}(E)$ obtained in the continuum Skyrme-HFB calculation with Green's function method are shown for the partial wave $f_{7/2}$ in ^{159}Sn, displayed with red solid lines.

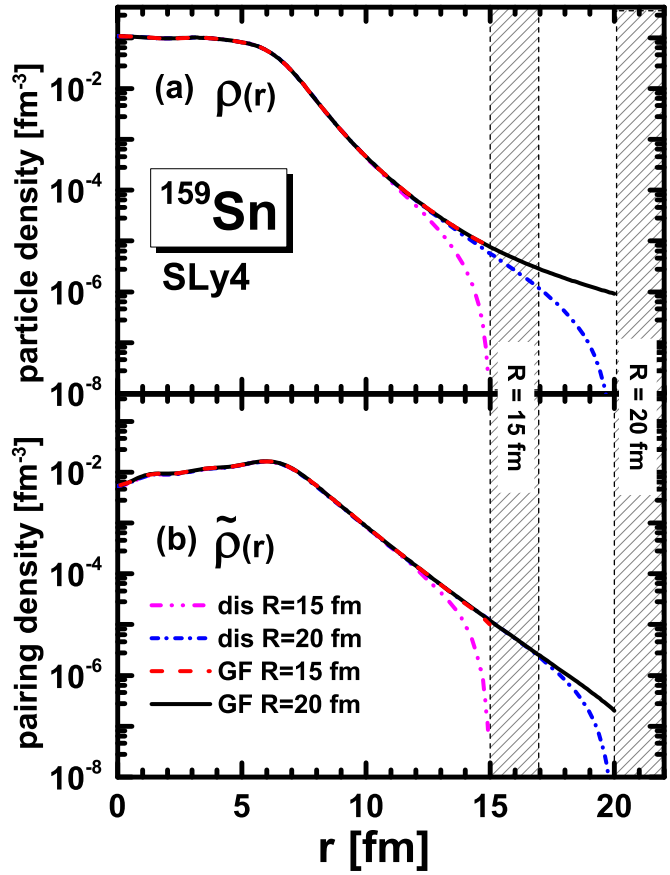

FIG. 3. (a) Neutron density $\rho_n(r)$ and (b) neutron pairing density $\tilde{\rho}_n(r)$ for ^{159}Sn by the continuum Skyrme-HFB theory with Green's function method, in comparison with those by the box-discretized method. Space sizes $R = 15$ fm and $R = 20$ fm are taken in both calculations. The Skyrme parameter set is SLy4.

For comparison, the occupation probability $v^2 \in [0, 1]$ and pair probability $uv \in [0, 0.25]$ in the box-discretized Skyrme-HFB calculations are also plotted,

$$v^2 = \int dr\, \varphi^2_{2,nlj}(r), \tag{31a}$$

$$uv = \int dr\, \varphi_{1,nlj}(r)\varphi_{2,nlj}(r), \tag{31b}$$

where $\varphi_{1,nlj}(r)$ and $\varphi_{2,nlj}(r)$ are respectively the upper and lower components of the HFB radial wave functions in Eq. (17a). From panel (a), two quasiparticle resonant peaks are observed in the continuum region around quasiparticle energies $E = 3.2$ and 27.6 MeV. Especially, the state near the continuum threshold $-\lambda$ corresponds to a weakly bound single-particle level $2f_{7/2}$ near the Fermi surface, which has an obvious width due to the couplings with the continuum, while the other peak corresponds to the deeply bound single-particle state $1f_{7/2}$, the occupation number density of which is very high and sharp. Correspondingly, the occupation probability v^2, denoted by blue dashed lines, is almost equal 1.0 for the deeply bound $1f_{7/2}$ while it is less than 1.0 for the weakly bound $2f_{7/2}$ state. However, a series of nonphysical

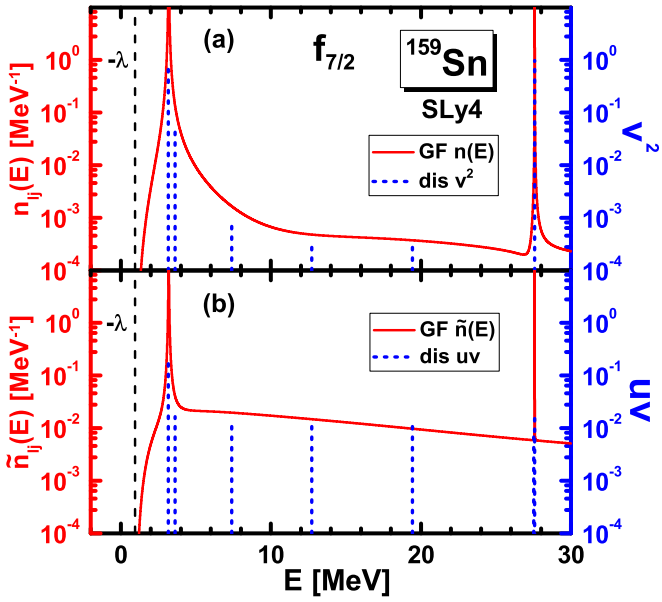

FIG. 4. (a) Occupation number density $n_{lj}(E)$ and (b) pair number density $\tilde{n}_{lj}(E)$ for the partial wave $f_{7/2}$ in ^{159}Sn obtained in the continuum Skyrme-HFB calculation with Green's function method (red solid lines). For comparison, the occupation probability v^2 and pair probability uv obtained in the box-discretzed Skyrme-HFB calculation are also plotted (blue dashed lines). The black dashed line denotes the continuum threshold $-\lambda$. The Skyrme parameter set is SLy4.

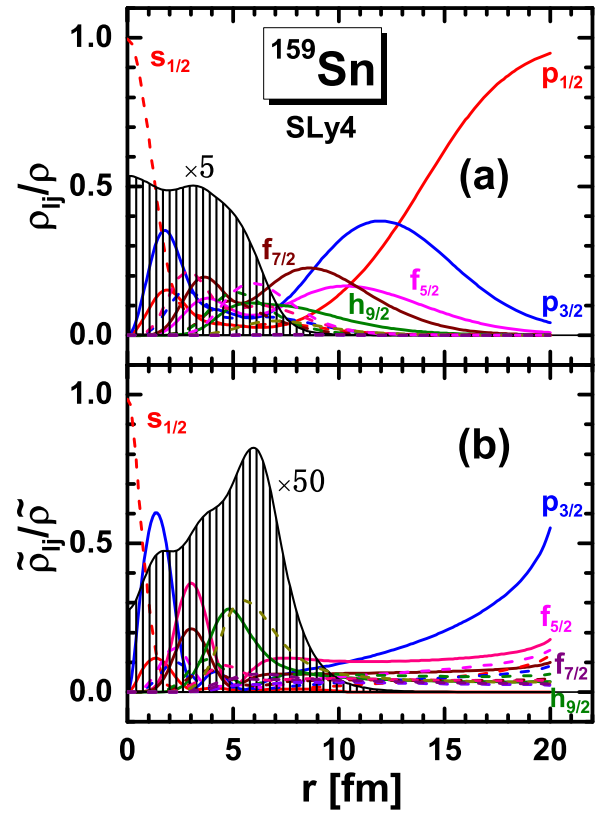

FIG. 5. Compositions of different partial waves to the total partial density $\rho_{lj}(r)/\rho(r)$ (a) and the total pair density $\tilde{\rho}_{lj}(r)/\tilde{\rho}(r)$ (b) for neutrons in nucleus ^{159}Sn by the continuum Skyrme-HFB calculations. The shallow regions corresponding to the particle density in the upper panel and the pair density in the lower panel are rescaled by multiplying a factor of 5 and 50, respectively.

discrete single-quasiparticle states are also obtained with the box-discretized HFB method. For example, the quasiparticle state $2f_{7/2}$ is discretized to three peaks by the box-discretized method. In panel (b), the pair number density $\tilde{n}_{lj}(E)$ distribution is similar to the occupation number density $n_{lj}(E)$, except the width is obviously smaller around the Fermi energy. In fact, it is believed that the pair number density $\tilde{n}_{lj}(E)$ represents more clearly the structure of continuum quasiparticle states due to the relevance to the pair correlation. From the occupation number density $n_{lj}(E)$ or the pair number density $\tilde{n}_{lj}(E)$, the quasiparticle energies and widths for the quasiparticle resonant states can be read directly. The pair correlation strength, the resonant states, and the couplings between the bound states and continuum can also be investigated by analyzing the resonant widths.

IV. RESULTS AND DISCUSSION

A. Halo in ^{159}Sn

In this part, still taking the neutron-rich nucleus ^{159}Sn as the example, we analyze its structure by the continuum Skyrme-HFB theory with blocking of the quasi-particle state $1p_{1/2}$. In Fig. 5, the particle density $\rho(r)$ and pair density $\tilde{\rho}(r)$ for neutrons in ^{159}Sn as well as their contributions from different partial waves lj, i.e., $\rho_{lj}(r)/\rho(r)$ and $\tilde{\rho}_{lj}(r)/\tilde{\rho}(r)$, are plotted as functions of radial coordinate r. The shallow regions are for the total densities $\rho(r)$ and $\tilde{\rho}(r)$. The solid and dashed lines are respectively the contributions from orbits with the negative and positive parities. In panel (a), the neutron density $\rho(r)$ decreases sharply from 5 fm and becomes very small around 9 fm, which finally determines the neutron radius in ^{159}Sn, $r_n = 5.44$ fm. Besides, it can be seen clearly that outside the nuclear surface, it is the orbits $p_{1/2}$, $p_{3/2}$, $f_{5/2}$, $f_{7/2}$, and $h_{9/2}$ that contribute a lot to the neutron density, especially the $p_{1/2}$ orbit, which is the most dominant composition in the large coordinate space with $r > 15$ fm. In panel (b), the pair density $\tilde{\rho}(r)$ mainly locates around the nuclear surface, becuase the pairing interaction mainly affects the orbits around the Fermi surface.

In Fig. 6, the occupation number densities $n_{lj}(E)$ and the pair number densities $\tilde{n}_{lj}(E)$ for neutrons in ^{159}Sn are plotted in the low energy interval $E = 0$–4 MeV. The dashed lines represent the continuum threshold with $|\lambda_n| = 0.958$ MeV, above which is the quasiparticle continuum. In panel (a), one discrete quasiparticle state $1p_{1/2}$ and five resonant states $1f_{5/2}$, $1p_{3/2}$, $1h_{9/2}$, $1i_{13/2}$, and $1f_{7/2}$ are observed. All those quasiparticle states correspond to the weakly bound or continuum single-particle states around the Fermi surface, as shown in Fig. 7. The blocked quasiparticle state $1p_{1/2}$, which locates below $|\lambda_n|$ with no width, corresponds to the weakly bound Hartree-Fock single-particle state $3p_{1/2}$. The quasiparticle resonant states $1f_{5/2}$, $1p_{3/2}$, $1h_{9/2}$, $1i_{13/2}$, and $1f_{7/2}$, which have peak structures with finite widths, correspond to the single-particle states $2f_{5/2}$, $3p_{3/2}$, $1h_{9/2}$, $1i_{13/2}$, and $3f_{7/2}$,

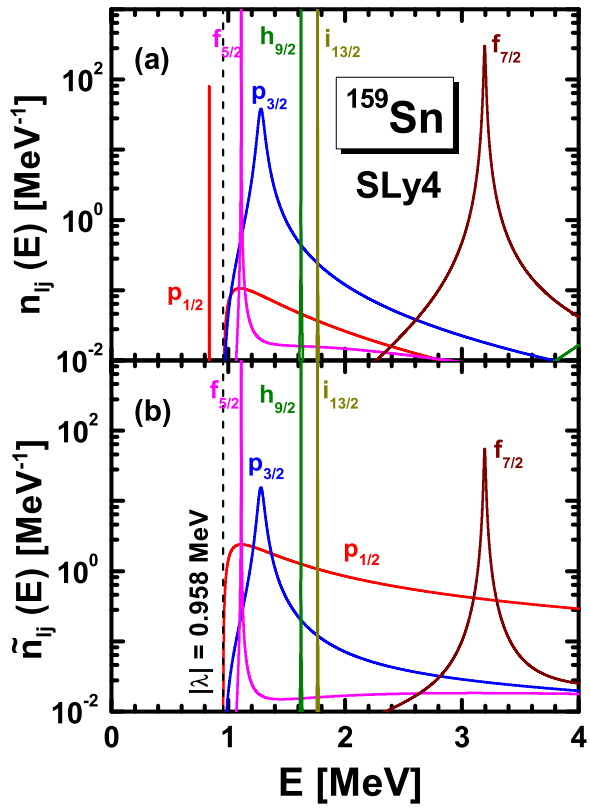

FIG. 6. (a) Neutron occupation number densities $n_{lj}(E)$ and (b) neutron pair number densities $\tilde{n}_{lj}(E)$ within quasiparticle energy range 0–4 MeV for different orbits lj in ^{159}Sn by continuum Skyrme-HFB calculations. The black dashed line represents the threshold of the quasiparticle continuum $E = -\lambda$.

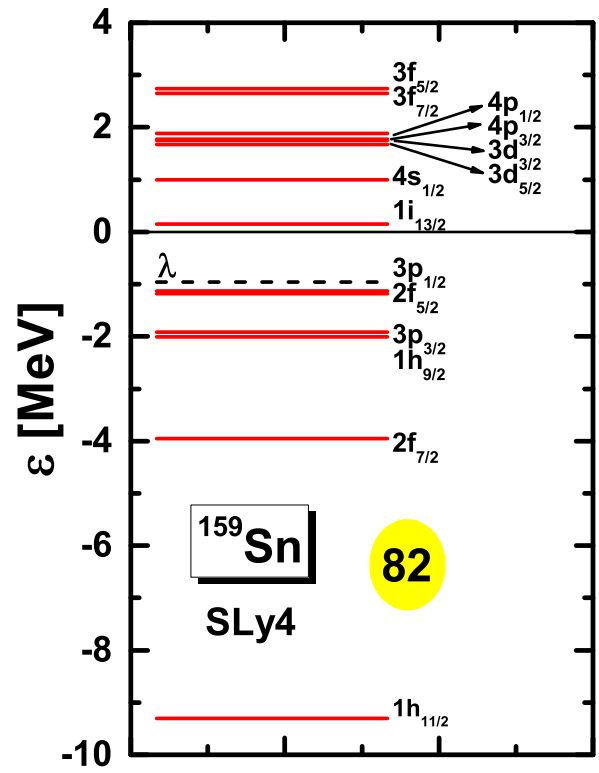

FIG. 7. Neutron Hartree-Fock single-particle energy ε of ^{159}Sn around the Fermi energy. The dashed line denotes the neutron Fermi energy λ. The Skyrme parameter set is SLy4.

respectively. All these single-particle states are bound except state $1i_{13/2}$. We can conclude that it is the pairing correlations that transform these bound HF single-particle orbits to the quasiparticle continuum and, the finite widths mainly result from the pair correlation and the couplings with the continuum. In general, the pair correlation will increase the width of resonant states [64]. From panel (a), the quasiparticle state $1p_{3/2}$ has the largest width, which is consistent with the most important contribution for the pair density $\tilde{\rho}(r)$ at coordinate space with $r > 10$ fm. The strict relations between the quasiparticle energy E and single-particle energy ε can be analyzed by the equation $E = \sqrt{(\varepsilon - \lambda)^2 + \Delta^2}$, where Δ is the pairing gap. Besides, we find that it is the states around the Fermi surface that contribute the extended density distributions Fig. 5. In panel (b), the discrete state $1p_{1/2}$ disappears in terms of the pair number density while other states keep the same positions.

B. Sn isotope

In the following, we take the neutron-rich Sn isotope as examples and investigate the halo structures. In Fig. 8, we plot the two-neutron separation energy $S_{2n}(N, Z) = E(N, Z) - E(N-2, Z)$ for both the even-even and odd-even Sn isotopes. The calculations are done using the Green's function method and the box-discretized method, which are denoted by the black filled circles and red open circles, respectively. It can be seen clearly that around the neutron gap $N = 82$, the two-neutron separation energy drops sharply from $S_{2n} = 13.25$ MeV at ^{132}Sn to $S_{2n} = 4.94$ MeV at ^{134}Sn, which is consistent with the experimental data [98]. After that, the S_{2n}

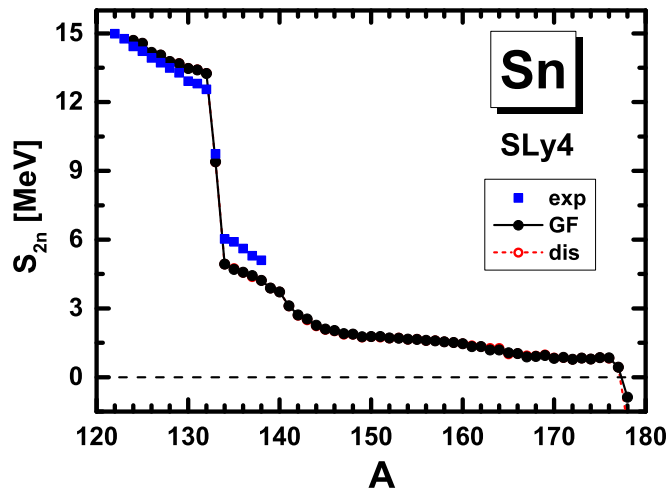

FIG. 8. Two-neutron separation energy S_{2n} obtained in the continuum (black filled circle) and box-discretized (red open circle) Skyrme-HFB calculations for the neutron-rich Sn isotopes with $A =$ 122–178. The experimental data [98] (blue filled square) are also presented for comparison.

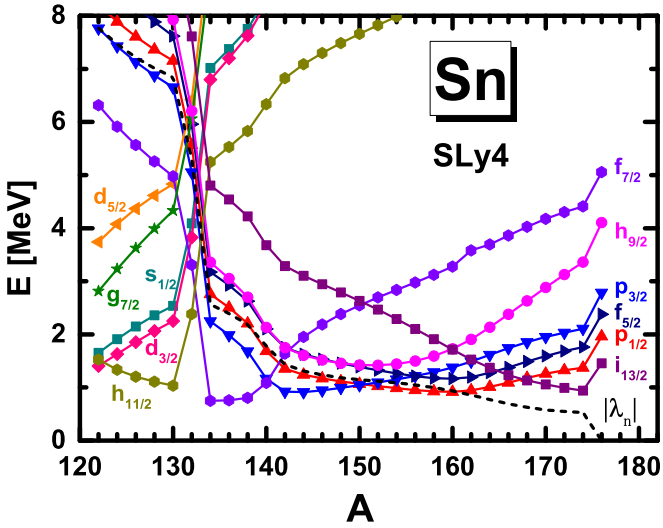

FIG. 9. Neutron quasiparticle levels around the continuum threshold obtained in the continuum Skyrme-HFB calculations for the Sn isotopes with $A = 122$–176. The dashed line represents the continuum threshold with $E = |\lambda_n|$.

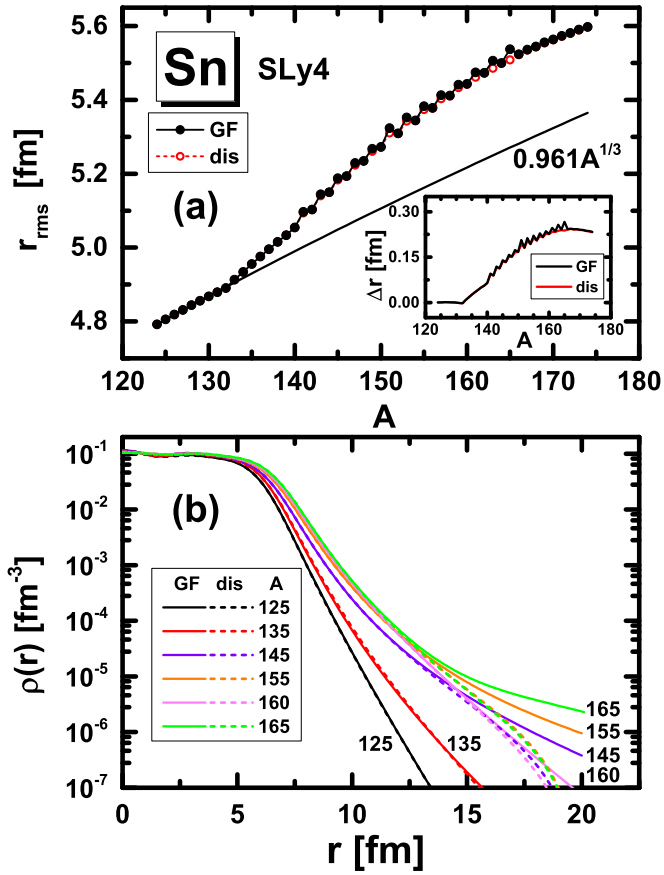

FIG. 10. (a) Neutron root-mean-square (rms) radius $r_{\rm rms}$ and (b) neutron density $\rho(r)$ for Sn isotopes. The filled circles and solid lines are the results of the continuum HFB calculations while the open circles and the dashed lines are those obtained in the box-discretized HFB calculations. In the inset of panel (a), the radius differences $\Delta r = r_{\rm rms} - 0.961\,A^{1/3}$ are shown.

decreases gradually and finally becomes negative at ^{178}Sn. In this way, the neutron drip-line nucleus of Sn isotopes is ^{177}Sn. However, the determination of the drip line is model dependent. Besides, according to different quantity or criterion, the drip line is also different. For example, according to the single-neutron separation energy $S_n(N,Z) = E(N,Z) - E(N-1,Z)$, the drip line of the Sn isotopes is much shorter and the drip line nucleus is ^{148}Sn; according to the Fermi surface λ_n shown in Fig. 9, the drip line nucleus is ^{174}Sn. The small two-neutron separation energy or the Fermi surface is one of the conditions for the emergence of the halo structure. From Fig. 8, we can see that the continuum and the box-discretized calculations give very close two-neutron separation energy S_{2n} and the same neutron drip line nucleus ^{177}Sn for the Sn isotopes. In comparison with the box-discretized method, the Green's function method has great advantages in describing the spatial properties of exotic nuclei such as densities and rms radius, as shown in Fig. 10.

In Fig. 9, the single quasiparticle levels around the continuum threshold $|\lambda_n|$ with quasiparticle energy $E = 0$–8 MeV are plotted as a function of the mass number A for the Sn isotopes. Around the continuum threshold, there are several quasiparticle orbits, i.e., $p_{1/2}$, $p_{3/2}$, $f_{5/2}$, $f_{7/2}$, $h_{9/2}$, and $i_{13/2}$, which correspond to the weakly bound single-particle levels or those in the continuum, as shown in Fig. 7. For the odd Sn isotopes, the last neutron occupies the lowest quasiparticle state, which gives the ground state of the system. As a result, in the odd mass nuclei $^{123\text{–}131}$Sn, $^{133\text{–}139}$Sn, $^{141\text{–}149}$Sn, $^{151\text{–}165}$Sn, and $^{167\text{–}173}$Sn, the last neutron is blocked in the orbit $h_{11/2}$, $f_{7/2}$, $p_{3/2}$, $p_{1/2}$, and $i_{13/2}$, respectively.

In Fig. 10, the neutron root-mean-square (rms) radius $r_{\rm rms}$,

$$r_{\rm rms} \equiv \sqrt{\frac{\int 4\pi r^4 \rho(r) dr}{\int 4\pi r^2 \rho(r) dr}}, \tag{32}$$

and the corresponding neutron density $\rho(r)$ are plotted for the neutron rich Sn isotopes. In panel (a), compared with the isotopic trend in $A \leqslant 132$, which gives an extrapolation as $r_{\rm rms} \approx 0.961\,A^{1/3}$ fm, the neutron rms radius in ^{133}Sn and the heavier isotopes display a steep increase with A. These results are consistent with the previous investigations for the even-even Sn isotopes in Refs. [28,99], where the halo structure is predicted in the isotopes with $A \geqslant 134$. In panel (b), the neutron densities of the odd mass nuclei ^{125,135,145,155,165}Sn are plotted as well as that of ^{160}Sn for comparison. The Sn isotopes with $A \geqslant 135$ exhibit a long tail extending far outside the nuclear surface compared with $A = 125$. Besides, compared with the box-discretized method, the Green's function method can describe well the extended density distributions in the very neutron-rich Sn isotopes, especially for those with $A \geqslant 145$.

After including the odd mass Sn isotopes, obvious odd-even staggering of the neutron radius $r_{\rm rms}$ is observed in the mass region $A = 151$–165. For example, the nucleus ^{151}Sn has a much larger neutron rms radius than the neighboring nuclei ^{150}Sn and ^{152}Sn. Correspondingly, the densities of those odd mass nuclei are much extended, such as those of the nuclei ^{145,155,165}Sn plotted in panel (b), which are more

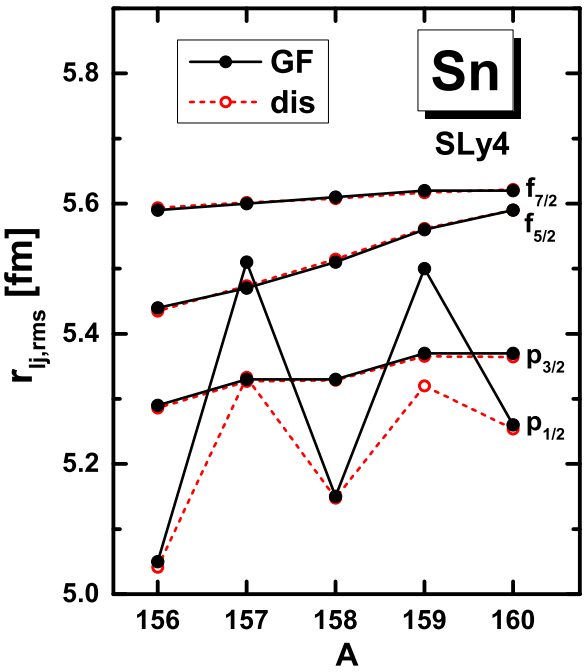

FIG. 11. Neutron rms radius $r_{\mathrm{rms},lj}$ of the $p_{1/2}$, $p_{3/2}$, $f_{5/2}$, and $f_{7/2}$ partial waves of Sn isotopes calculated for the lj-decomposed neutron density $\rho_{lj}(r)$. The filled symbols are obtained in the continuum Skyrme-HFB calculation while the open symbols are obtained in the box-discretized Skyrme-HFB calculation.

extended than the even-even nuclei. Moreover, this odd-even staggering is much more strongly described by the Green's function method than by the box-discretized method. This is mainly due to the larger rms radii of the odd mass isotopes obtained by the Green's function method. For the same reason, the odd-even staggering of the neutron rms radius cannot be observed in the mass region $A = 155$–165 by the box-discretized method. In order to see better the differences of the rms radii obtained by the continuum and the box-discretized methods, we plot $r_{\mathrm{rms}} - 0.961\,A^{1/3}$ by the two methods in the inset of panel (a). It is shown that the Green's function method obtains larger rms radii for the odd mass nuclei from ^{141}Sn to ^{165}Sn compared with the box-discretized method.

To further investigate the odd-even staggering in Fig. 10, the contributions of the neutron rms radius from different partial waves $r_{lj,\mathrm{rms}}$ are studied,

$$r_{lj,\mathrm{rms}} \equiv \sqrt{\frac{\int 4\pi r^4 \rho_{lj}(r) dr}{\int 4\pi r^2 \rho_{lj}(r) dr}}, \tag{33}$$

where $\rho_{lj}(r)$ is the density of the partial wave lj. In Fig. 11, we plot the rms radius for partial waves $lj = p_{1/2}$, $p_{3/2}$, $f_{5/2}$, and $f_{7/2}$ in nuclei $^{156\text{–}160}$Sn. Results obtained in the continuum HFB calculations and box-discretized HFB calculations are shown by the filled symbols and open symbols, respectively. We can see clearly that the large rms radii of ^{157}Sn and ^{159}Sn compared with those of neighboring nuclei are mainly due to the large contribution from the $p_{1/2}$ partial wave, which is the blocked state of the odd neutron. Meanwhile, the rms radii for other partial waves of Sn isotopes do not exhibit large odd-even staggering. Comparing the results obtained by the Green's function method and box-discretized method, the rms radii of the partial wave $p_{1/2}$ are very different for the odd mass Sn isotopes, while they are quit close for the even-even Sn isotopes. More precisely, it is the occupation of the very weakly bound $3p_{1/2}$ state in the odd mass Sn isotopes that leads to the large rms radius of partial wave $p_{1/2}$. Since the Green's function method can describe the weakly bound state and the continuum very well, it finally gives much a larger rms radius of the $p_{1/2}$ partial wave.

V. SUMMARY

In this work, the self-consistent continuum Skyrme-HFB theory is extended to describe odd-A nuclei with the Green's function technique in the coordinate space. The blocking effects are incorporated by taking the equal filling approximation. Detailed formulas for the densities and quasiparticle spectrum in forms of the HFB Green's function are presented for odd nuclear systems.

Taking the neutron-rich nucleus ^{159}Sn as an example, we give numerical details and checks. The SLy4 parameter is taken in the particle-hole channel and the DDDI is taken as the pairing interaction, the parameters of which are constrained by reproducing the experimental neutron pairing gaps for the Sn isotopes and the scattering length $a = -18.5$ fm in the ^1S channel of the bare nuclear force. To perform the integrals of the Green's function, three contour paths $C_{E<0}$, C_{b}^{-}, and C_{b}^{+} are chosen, the heights of which are taken uniformly as $\gamma = 0.1$ MeV, and width $C_{E<0}$ is taken as the maximal quasiparticle energy $E_{\mathrm{cut}} = 60$ MeV to enclose all the negative quasiparticle energies. The numerical checks on the widths of contour paths C_{b}^{-} and C_{b}^{+} introduced for the blocking effects are discussed, and it is found that the width E_{b} should taken with $E_{i_{\mathrm{b}}} < E_{\mathrm{b}} < -\lambda$. This means that the contour paths C_{b}^{-} and C_{b}^{+} should include the blocked quasiparticle state but cannot intrude into the continuum area. Besides, by comparing with the box-discretized Skyrme-HFB calculations, the advantages of the Green's function method in describing the neutron-rich nuclei are shown. First, Green's function method can describe the extended density distributions very well, and these descriptions are independent of the space size. Second, the Green's function method can describe the quasiparticle spectrum, especially the continuum, very well; thereby the energies and widths of quasiparticle resonant states can be given directly.

To study the halo structure, we first investigate the neutron-rich nucleus ^{159}Sn with the continuum Skyrme-HFB theory by blocking the quasiparticle state $1p_{1/2}$. We find that it is the weakly bound states $3p_{1/2}$, $2f_{5/2}$, $3p_{3/2}$, $1h_{9/2}$, and $2f_{7/2}$ that contribute a lot to the extended density distributions at large coordinate space. Besides, the particle number density $n_{lj}(E)$ and pair number density $\tilde{n}_{lj}(E)$ are also studied, from which the quasiparticle energies and the width of resonant states can be extracted. The pairing correlation and the couplings with the continuum can be analyzed from the widths of quasiparticle resonant states.

Finally, taking the neutron-rich Sn isotope with mass number $A = 122$–178 as examples, the halo structures are studied

systematically. After exceeding the shell $N = 82$, the two-neutron separation energy S_{2n} of Sn isotopes decreases sharply and keeps a small value in a long mass range, which offers a good environment for the emergence of the halo structure together with the low Fermi energy. Compared with the traditional trend of $r = 0.961\,A^{1/3}$ fm, the neutron rms radius in ^{133}Sn and the heavier isotopes display a steep increase with A. Correspondingly, the densities for those nuclei are very extended. Besides, the odd-even staggering of neutron radius $r_{\rm rms}$ is observed in the mass region $A = 151$–165, in which the last neutron of the odd nucleus is blocked in the low l orbit $p_{1/2}$ or $p_{3/2}$. Moreover, this odd-even staggering is much more strongl described by the Green's function method than by the box-discretized method, due to the advantage of the Green's function method in describing the weakly bound state and the continuum.

ACKNOWLEDGMENTS

T.-T.S. is grateful to Prof. J. Meng, Prof. M. Matsuo, and Dr. Y. Zhang for fruitful discussions. This work was supported by the National Natural Science Foundation of China (Grants No. 11505157 and No. 11705165).

[1] J. Xia, W. Zhan, B. Wei, Y. Yuan, M. Song, W. Zhang, X. Yang, P. Yuan, D. Gao, H. Zhao *et al.*, Nucl. Instrum. Methods Phys. Res., Sect. A **488**, 11 (2002).
[2] W. L. Zhan, H. S. Xu, G. Q. Xiao, J. W. Xia, H. W. Zhao, and Y. Yuan, Nucl. Phys. A **834**, 694c (2010).
[3] C. Sturm, B. Sharkov, and H. Stöcker, Nucl. Phys. A **834**, 682c (2010).
[4] S. Gales, Nucl. Phys. A **834**, 717c (2010).
[5] T. Motobayashi, Nucl. Phys. A **834**, 707c (2010).
[6] M. Thoennessen, Nucl. Phys. A **834**, 688c (2010).
[7] S. Choi, in *KoRIA project - RI accelerator in Korea*, International Symposium on Nuclear Physics in Asia, 14–15 October 2010 (Beihang University, Beijing, 2010).
[8] A. C. Mueller and B. M. Sherrill, Annu. Rev. Nucl. Part. Sci. **43**, 529 (1993).
[9] I. Tanihata, Prog. Part. Nucl. Phys. **35**, 505 (1995).
[10] P. G. Hansen, A. S. Jensen, and B. Jonson, Annu. Rev. Nucl. Part. Sci. **45**, 591 (1995).
[11] R. F. Casten and B. M. Sherrill, Prog. Part. Nucl. Phys. **45**, S171 (2000).
[12] C. A. Bertulani, M. S. Hussein, and G. Munzenberg, *Physics of Radioactive Beams* (Nova Science, New York, 2001).
[13] B. Jonson, Phys. Rep. **389**, 1 (2004).
[14] A. S. Jensen, K. Riisager, D. V. Fedorov, and E. Garrido, Rev. Mod. Phys. **76**, 215 (2004).
[15] S. N. Ershov, L. V. Grigorenko, J. S. Vaagen, and M. V. Zhukov, J. Phys. G: Nucl. Phys. **37**, 064026 (2010).
[16] Z. X. Cao and Y. L. Ye, Sci. China Phys. Mech. Astron. **54**, 1 (2011).
[17] I. Tanihata, H. Hamagaki, O. Hashimoto, Y. Shida, N. Yoshikawa, K. Sugimoto, O. Yamakawa, T. Kobayashi, and N. Takahashi, Phys. Rev. Lett. **55**, 2676 (1985).
[18] T. Minamisono, T. Ohtsubo, I. Minami, S. Fukuda, A. Kitagawa, M. Fukuda, K. Matsuta, Y. Nojiri, S. Takeda, H. Sagawa *et al.*, Phys. Rev. Lett. **69**, 2058 (1992).
[19] W. Schwab, H. Geissel, H. Lenske, K. H. Behr, A. Brünle, K. Burkard, H. Irnich, T. Kobayashi, G. Kraus, A. Magel *et al.*, Z. Phys. A **350**, 283 (1995).
[20] J. Meng and P. Ring, Phys. Rev. Lett. **77**, 3963 (1996).
[21] J. Meng and P. Ring, Phys. Rev. Lett. **80**, 460 (1998).
[22] S.-G. Zhou, J. Meng, P. Ring, and E.-G. Zhao, Phys. Rev. C **82**, 011301(R) (2010).
[23] A. Ozawa, T. Kobayashi, T. Suzuki, K. Yoshida, and I. Tanihata, Phys. Rev. Lett. **84**, 5493 (2000).
[24] P. Adrich, A. Klimkiewicz, M. Fallot, K. Boretzky, T. Aumann, D. Cortina-Gil, U. Datta Pramanik, T. W. Elze, H. Emling, H. Geissel *et al.* (LAND-FRS Collaboration), Phys. Rev. Lett. **95**, 132501 (2005).
[25] J. Dechargé and D. Gogny, Phys. Rev. C **21**, 1568 (1980).
[26] J. Dobaczewski, H. Flocard, and J. Treiner, Nucl. Phys. A **422**, 103 (1984).
[27] J. Dobaczewski, W. Nazarewicz, T. R. Werner, J. F. Berger, C. R. Chinn, and J. Dechargé, Phys. Rev. C **53**, 2809 (1996).
[28] S. Mizutori, J. Dobaczewski, G. A. Lalazissis, W. Nazarewicz, and P.-G. Reinhard, Phys. Rev. C **61**, 044326 (2000).
[29] M. Grasso, N. Sandulescu, N. Van Giai, and R. J. Liotta, Phys. Rev. C **64**, 064321 (2001).
[30] J. Meng, Nucl. Phys. A **635**, 3 (1998).
[31] J. Meng, H. Toki, S. G. Zhou, S. Q. Zhang, W. H. Long, and L. S. Geng, Prog. Part. Nucl. Phys. **57**, 470 (2006).
[32] D. Vretenar, A. V. Afanasjev, G. A. Lalazissis, and P. Ring, Phys. Rep. **409**, 101 (2005).
[33] W. Pöschl, D. Vretenar, G. A. Lalazissis, and P. Ring, Phys. Rev. Lett. **79**, 3841 (1997).
[34] W. H. Long, P. Ring, N. Van Giai, and J. Meng, Phys. Rev. C **81**, 024308 (2010).
[35] W. H. Long, P. Ring, J. Meng, N. Van Giai, and C. A. Bertulani, Phys. Rev. C **81**, 031302(R) (2010).
[36] X. L. Lu, B. Y. Sun, and W. H. Long, Phys. Rev. C **87**, 034311 (2013).
[37] L.-L. Li, J. Meng, P. Ring, E.-G. Zhao, and S.-G. Zhou, Phys. Rev. C **85**, 024312 (2012).
[38] L.-L. Li, J. Meng, P. Ring, E.-G. Zhao, and S.-G. Zhou, Chin. Phys. Lett. **29**, 042101 (2012).
[39] Y. Chen, L. Li, H. Liang, and J. Meng, Phys. Rev. C **85**, 067301 (2012).
[40] X. X. Sun, J. Zhao, and S. G. Zhou, Phys. Lett. B **785**, 530 (2018).
[41] J. C. Pei, Y. N. Zhang, and F. R. Xu, Phys. Rev. C **87**, 051302(R) (2013).
[42] Y. N. Zhang, J. C. Pei, and F. R. Xu, Phys. Rev. C **88**, 054305 (2013).
[43] C. Horowitz and B. D. Serot, Nucl. Phys. A **368**, 503 (1981).
[44] W. H. Press, S. A. Teukolsky, W. T. Vetterling, and B. P. Flannery, *Numerical Recipes in Fortran 77: The Art of Scientific Computing*, Vol. 1 of Fortran Numerical Recipes (Cambridge University Press, Cambridge, 1992).
[45] Y. Gambhir, P. Ring, and A. Thimet, Ann. Phys. (NY) **198**, 132 (1990).

[46] M. V. Stoitsov, W. Nazarewicz, and S. Pittel, Phys. Rev. C **58**, 2092 (1998).
[47] S.-G. Zhou, J. Meng, and P. Ring, Phys. Rev. C **68**, 034323 (2003).
[48] K. Bennaceur, J. Dobaczewski, and M. Ploszajczak, Phys. Lett. B **496**, 154 (2000).
[49] S. T. Belyaev, A. V. Smirnov, S. V. Tolokonnikov, and S. A. Fayans, Sov. J. Nucl. Phys. **45**, 783 (1987).
[50] E. Tamura, Phys. Rev. B **45**, 3271 (1992).
[51] D. L. Foulis, Phys. Rev. A **70**, 022706 (2004).
[52] E. N. Economou, *Green's Fucntion in Quantum Physics* (Springer-Verlag, Berlin, 2006).
[53] M. Matsuo, Nucl. Phys. A **696**, 371 (2001).
[54] M. Matsuo, Prog. Theor. Phys. Suppl. **146**, 110 (2002).
[55] M. Matsuo, K. Mizuyama, and Y. Serizawa, Phys. Rev. C **71**, 064326 (2005).
[56] M. Matsuo, Y. Serizawa, and K. Mizuyama, Nucl. Phys. A **788**, 307 (2007).
[57] Y. Serizawa and M. Matsuo, Prog. Theor. Phys. **121**, 97 (2009).
[58] K. Mizuyama, M. Matsuo, and Y. Serizawa, Phys. Rev. C **79**, 024313 (2009).
[59] M. Matsuo and Y. Serizawa, Phys. Rev. C **82**, 024318 (2010).
[60] H. Shimoyama and M. Matsuo, Phys. Rev. C **84**, 044317 (2011).
[61] H. Shimoyama and M. Matsuo, Phys. Rev. C **88**, 054308 (2013).
[62] M. Matsuo, Phys. Rev. C **91**, 034604 (2015).
[63] Y. Zhang, M. Matsuo, and J. Meng, Phys. Rev. C **83**, 054301 (2011).
[64] Y. Zhang, M. Matsuo, and J. Meng, Phys. Rev. C **86**, 054318 (2012).
[65] X. Y. Qu and Y. Zhang, Phys. Rev. C **99**, 014314 (2019).
[66] H. Oba and M. Matsuo, Phys. Rev. C **80**, 024301 (2009).
[67] J. Daoutidis and P. Ring, Phys. Rev. C **80**, 024309 (2009).
[68] D. Yang, L.-G. Cao, Y. Tian, and Z.-Y. Ma, Phys. Rev. C **82**, 054305 (2010).
[69] B. D. Sert and J. D. Walecka, Adv. Nucl. Phys. **16**, 1 (1986).
[70] J. Meng and S.-G. Zhou, J. Phys. G: Nucl. Part. Phys. **42**, 093101 (2015).
[71] W. Zhang, Z. P. Li, and S. Q. Zhang, Phys. Rev. C **88**, 054324 (2013).
[72] W. Zhang and Y.-F. Niu, Chin. Phys. C **41**, 094102 (2017).
[73] W. Zhang and Y. F. Niu, Phys. Rev. C **96**, 054308 (2017).
[74] W. Zhang and Y. F. Niu, Phys. Rev. C **97**, 054302 (2018).
[75] T.-T. Sun, E. Hiyama, H. Sagawa, H.-J. Schulze, and J. Meng, Phys. Rev. C **94**, 064319 (2016).
[76] W.-L. Lu, Z.-X. Liu, S.-H. Ren, W. Zhang, and T.-T. Sun, J. Phys. G: Nucl. Part. Phys. **44**, 125104 (2017).
[77] T.-T. Sun, W.-L. Lu, and S.-S. Zhang, Phys. Rev. C **96**, 044312 (2017).
[78] T.-T. Sun, C.-J. Xia, S.-S. Zhang, and M. S. Smith, Chin. Phys. C **42**, 025101 (2018).
[79] Z.-X. Liu, C.-J. Xia, W.-L. Lu, Y.-X. Li, J.-N. Hu, and T. T. Sun, Phys. Rev. C **98**, 024316 (2018).
[80] C.-J. Xia, G.-X. Peng, T.-T. Sun, W.-L. Guo, D.-H. Lu, and P. Jaikumar, Phys. Rev. D **98**, 034031 (2018).
[81] T.-T. Sun, S.-S. Zhang, Q.-L. Zhang, and C.-J. Xia, Phys. Rev. D **99**, 023004 (2019).
[82] T.-T. Sun, W.-L. Lu, L. Qian, and Y.-X. Li, Phys. Rev. C **99**, 034310 (2019).
[83] B. Sun, F. Montes, L. S. Geng, H. Geissel, Yu. A. Litvisnov, and J. Meng, Phys. Rev. C **78**, 025806 (2008).
[84] Z. M. Niu, B. H. Sun, and J. Meng, Phys. Rev. C **80**, 065806 (2009).
[85] X. D. Xu, B. Sun, Z. M. Niu, Z. Li, Y. Z. Qian, and J. Meng, Phys. Rev. C **87**, 015805 (2013).
[86] Z. M. Niu, Y. F. Niu, H. Z. Liang, W. H. Long, T. Nikšić, D. Vretenar, and J. Meng, Phys. Lett. B **723**, 172 (2013).
[87] J. S. Zheng, N. Y. Wang, Z. Y. Wang, Z. M. Niu, Y. F. Niu, and B. Sun, Phys. Rev. C **90**, 014303 (2014).
[88] T. T. Sun, S. Q. Zhang, Y. Zhang, J. N. Hu, and J. Meng, Phys. Rev. C **90**, 054321 (2014).
[89] T. T. Sun, Z. M. Niu, and S. Q. Zhang, J. Phys. G: Nucl. Part. Phys. **43**, 045107 (2016).
[90] S.-H. Ren, T. T. Sun, and W. Zhang, Phys. Rev. C **95**, 054318 (2017).
[91] T. T. Sun, Sci. Sin.-Phys. Mech. Astron. **46**, 12006 (2016).
[92] S. Shlomo and G. Bertsch, Nucl. Phys. A **243**, 507 (1975).
[93] P. Ring and P. Schuck, *The Nuclear Many-Body Problem* (Springer-Verlag, Berlin, 2000).
[94] Y. M. Engel, D. M. Brink, K. Goeke, S. J. Krieger, and D. Vautherin, Nucl. Phys. A **249**, 215 (1975).
[95] M. Bender, P.-H. Heenen, and P.-G. Reinhard, Rev. Mod. Phys. **75**, 121 (2003).
[96] E. Chabanat, P. Bonche, P. Haensel, J. Meyer, and R. Schaeffer, Nucl. Phys. A **635**, 231 (1998).
[97] M. Matsuo, Phys. Rev. C **73**, 044309 (2006).
[98] M. Wang, G. Audi, A. H. Wapstra, F. G. Kongdev, M. MacCormick, X. Xu, and B. Pfeiffer, Chin. Phys. C **36**, 1603 (2012).
[99] V. Rotival and T. Duguet, Phys. Rev. C **79**, 054308 (2009).